Tuned inerter dampers with linear hysteretic damping.

DEASTRA, Predaricka <http://orcid.org/0000-0002-1709-4686>, WAGG, David, SIMS, Neil and AKBAR, Mahesa

Received: 3 October 2019 | Revised: 16 March 2020 | Accepted: 26 April 2020

DOI: 10.1002/eqe.3287

RESEARCH ARTICLE

WILEY

Tuned inerter dampers with linear hysteretic damping

Predaricka Deastra | **David Wagg** | **Neil Sims** | **Mahesa Akbar**

Department of Mechanical Engineering, The University of Sheffield, Sheffield, UK

Correspondence
Predaricka Deastra, Department of Mechanical Engineering, The University of Sheffield, S1 3JD Sheffield, UK.
Email: pdeastra1@sheffield.ac.uk

Funding information
Indonesia Endowment Fund For Education, Grant/Award Number: 20160422015904

Summary

This paper explores the influence of linear hysteretic damping on the performance of passive tuned-inerter devices. An inerter is a device that produces a force proportional to the relative acceleration across its two terminals; devices incorporating inerters have received widespread attention in the earthquake engineering community, because they offer the ability to improve the seismic response of structures. However, the majority of this research has assumed that the damping components within the tuned-inerter device exhibit viscous, rather than hysteretic, damping. This restriction imposes an essential question on how the hysteretic damping model will change the performance of the device compared with the viscous damping model. It is shown that the response of viscous and hysteretic inerter systems have significant differences in displacement amplitude due to the frequency dependency of the damping. Therefore, a new formulation for obtaining the optimum loss factor of the hysteretic damping in the inerter system is proposed. Next, the challenges associated with accurately predicting the time-response of a hysteretically damped system are discussed. A numerical time-integration method is extended to address these challenges, using a new formulation that has the benefit of being broadly applicable to multidegree-of-freedom hysteretic linear systems and nonstationary random signals. The results show that the earthquake responses from the hysteretic damping model can differ significantly from the ones obtained via the viscous model.

KEYWORDS

linear hysteretic damping, optimum loss factor, passive tuned-inerter devices, seismic response, time-response

1 | INTRODUCTION

In 1997, Okumura Atsushi[1] patented the so-called gyro-mass device, which operated in parallel with a spring and a damper. This gyro-mass, consisting of two disks acting as inertia elements, rotated on a geared rod in such a way that the force generated by the gyro-mass, F, is equivalent to the relative acceleration between its two terminals, x_A and x_B. This relation can be expressed as

$$F = b_d(\ddot{x}_A - \ddot{x}_B), \tag{1}$$

where

$$b_d = J/{r_d}^2. \tag{2}$$

Here, J is the moment inertia of the disks, and r_d is the distance from the centre of the disks to the point where the rod is attached (otherwise called the radius of gyration). The parameter b_d is called the inertance, which is measured in kilogram, and can in fact be achieved by several mechanisms, such as rotational motion of a flywheel[2] or fluid flow.[3] Following this initial concept, several other types of gyro-mass or inerter devices have been proposed. Smith[4] developed an inerter, consisting of flywheel, rack, pinions and gears. The force generated by these types of inerter can be expressed in the same way as Equation (1). Recently, many studies on the realisation of this inerter concept have been conducted based on three main mechanisms: mechanical geared, ball screw and fluid-based inerters.[5-9]

The application of the inerter for vibration suppression in civil engineering structures has been studied by proposing several configurations of three basic elements: inerter, viscous damper and spring (or equivalent stiffness element). One of the first inerter-damper configurations to be introduced was the tuned-viscous-mass-damper (TVMD), described in detail in Ikago et al.[2] The damper consists of a parallel-connected ball-screw inerter-viscous damper in series with a spring element. Of particular note is that a device of this type has been put into service in a real structure.[10] The generalisation of this device layout is called a parallel-connected-viscous-inerter-damper (PVID). For example, Pan et al.[11] derived the optimum solution for the PVID in a damped single-degree-of-freedom (SDOF) structure with a numerical optimisation technique, using allowable parametric bounds. More recently, the feasibility of using the PVID concept for vibration suppression of civil structures using a fluid inerter has been studied.[12,13]

Lazar et al.[14] proposed a tuned-inerter-damper (TID) for vibration suppression of civil engineering structures. The TID consists of a parallel connected spring and viscous damper in series with an inerter. This arrangement is similar to that of a tuned-mass-damper (TMD) with the mass element being replaced by an inerter. The TID has been proven to have similar performance to the TMD for the targeted resonance, but it also offers additional benefits compared with the TMD. As is well known, the TMD typically requires a large amount of mass to provide a large mass ratio and to achieve optimum performance. For the same mass ratio, the actual mass of the TID is far less than that of the TMD because the inerter element can produce inertance several times higher than its physical mass.[4] Additionally, it has been also shown that the TID achieves its best performance when placed at the base of the main structure, which is contrary to the TMD which must be placed at the top of the structure, where the maximum displacements occur. To obtain its optimum damping parameter, Lazar et al.[14] proposed a tuning rule that is based on the fixed-point theory by Den Hartog[15] for the TMD. In a similar manner, Hu et al.[16] studied five configurations employing an inerter including the TID layout and gave a tuning example for each of them when attached to an undamped SDOF structure. More recently, the TID has been studied for vibration suppression of cables[17] and for enhancing the performance of base-isolated structures subjected to earthquake base-excitation.[18,19]

Marian and Giaralis[20] proposed an alternative device called a tuned-mass-damper-inerter (TMDI). The device consists of a traditional TMD with an inerter attached to the mass element. The advantage of the device is its capability of reducing the total mass of the TMD. The concept of changing the inertance by using a control system to provide larger mass ratio has also been investigated.[21] The frequency of the TMD can be easily tuned to fit the frequency of the excitations. Optimal design of the TMDI for dynamic vibration suppression by assuming white noise process as base input was studied by Pietrosanti et al.[22] The TMDI has also been studied for application to base-isolated structures.[23,24]

Following the initial analytical studies on the application of inerter-based dampers for vibration suppression of civil structures, a selection of experimental studies have been conducted in order to validate those well established concepts. Brzeski et al.[25] conducted an experimental study of the TMDI on an SDOF system. An experimental study of a PVID concept using a mechanical geared inerter can be found in Hessabi and Mercan.[26] More recently, Hessabi[27] conducted experimental work testing a mechanical geared inerter-based damper for vibration suppression of a civil structure using the real-time hybrid simulation method.

Despite the successful studies of the inerter-based damper systems both analytically and experimentally, many research questions remain. In particular, models such as Equation (1) are highly idealised, and as the development of these concepts progress, it is important to have models that can capture more physically realistic cases. For example, some studies have suggested the importance of considering the nonlinearities of both the damping and the inerter devices. Buelga et al.,[28] amongst others,[29-31] studied the effect of the ball-screw inerter nonlinearity on the performance of the structure to which the inerter is attached.

This paper proposes the use of the hysteretic damping as a new alternative to viscous damping in the idealised inerter-based damper model, and in particular, we will focus on the tuned-inerter-hysteretic-damper (TIhD) and the tuned-mass-hysteretic-damper-inerter (TMhDI). Hysteretic damping has the benefit of smaller response amplitude amplification at higher vibration frequencies due to its energy dissipation being frequency independent. Systems of this

type have been studied extensively.[32-35] The hysteretic damping model also better describes the behaviour of certain materials.[36] Mathematically, one of the most frequently used ways of modelling hysteretic damping is as part of a complex stiffness function, which has the problem of noncausality—an issue that shall be discussed in detail below.

Equivalent viscous damping discussed in Chopra[37] has been widely used to model the loss factor or damping in the complex stiffness case. However, it is well known that for both single-degree-of-freedom (SDOF) and multi-degree-of-freedom (MDOF) systems, that is, civil structures, the use of equivalent viscous damping may only be valid for a particular frequency range near the frequency of interest, which is usually the resonance frequency.[38]

In addition, concerning a nonharmonic excitation case, such as earthquake inputs, it is essential to evaluate the structural response in a time-domain basis rather than a frequency-domain basis. Therefore, in the present work, we investigate the hysteretic damping by developing a new method in a time domain.

The noncausal nature of the complex stiffness function leads to the occurrence of unstable poles in the time domain analysis of the system. As a result, implementing this type of model is not as straightforward as the viscous model. The idea of a causal hysteretic element has been developed as an alternative,[39] although this too has significant difficulties with computation.[40] To deal with the unstable poles issue, several methods have been proposed in the case of SDOF systems.

The use of analytic signals, along with the Hilbert transform and a time reversal technique, is one of the first methods introduced to solve such systems in the time domain; see Inaudi and Makris.[41] In this paper, the method of Inaudi and Makris[41] is modified in order to solve the time domain response of the structures with TIhD and TMhDI. This modification takes advantage of some key simplifying assumptions that are justified for the types of system under consideration. As a result, the proposed method makes it possible to solve the problem using standard numerical integration algorithms such as the Runga–Kutta family of solvers that are available within MATLAB, rather than the more specialist methods required previously. A discussion about the method is presented in Section 3.

A recent investigation in Málaga-Chuquitaype et al.[42] presented material modelling of an inerter damping system by means of finite elements. Both SDOF and MDOF systems were investigated, and responses of harmonic excitations and earthquake cases were evaluated. However, for a preliminary design stage, numerical simulation via finite element analysis could be computational costly. Hence, the present numerical method via Hilbert transform and time-reversal technique is proposed and implemented to support analysis on TIhD and TMhDI designs. Both the TIhD and TMhDI use a hysteretic damping element instead of a viscous damper. The motivation for using this damping model is to try and more accurately represent the case when a material damping (e.g., rubberised component) is present in the inerter-based device. When the mass of the inerter is also included in the model, then the TMhDI model becomes more appropriate. It should be also noted that in this work, both TIhD/TMhDI and the host structure are assumed linear. This is an important assumption of the models used in this paper.

The TMhDI has a small secondary mass between the inerter and the complex damping elements, analogous to the TMDI concept. In this paper, the secondary mass is considered to be approximately 5% of the inertance, to represent the mass of the inerter device only. The idea is that this TMhDI will capture both the effects of the inerter mass and the hysteretic damping and therefore offer a potentially more physically realistic model than the idealised concepts of the TID and the TMDI.

2 | ANALYTICAL MODELLING AND OPTIMISATION

A generalised model of a n-DOF lumped mass system is shown in Figure 1. The structure is separated into three parts: bottom storey, $i = 1$; middle storeys, i^{th}, where $i \in [2 : n-1]$; and top storey, $i = n$. In this study, the performance comparison of four different inertial damper systems when placed at the bottom story level was examined. As a well established concept, the TID was used as a benchmark to the performance of the other devices. The TMDI was studied to see the effect of the small additional mass element in the TID. Then the TIhD and TMhDI were studied to gain insight into the effect of hysteretic damping.

The equations of motion of the n-DOF structure as shown in Figure 1 in absolute coordinates can be written as

$$\begin{cases} (m_1 s^2 + k_{0,1} + k_{1,2})X_1 = k_{1,2}X_2 + k_{0,1}R + F_{1,0} \\ \vdots \\ (m_i s^2 + k_{i-1,i} + k_{i,i+1})X_i = k_{i-1,i}X_{i-1} + k_{i,i+1}X_{i+1} \\ \vdots \\ (m_n s^2 + k_{n-1,n})X_n = k_{n-1,n}X_{n-1} \end{cases} \tag{3}$$

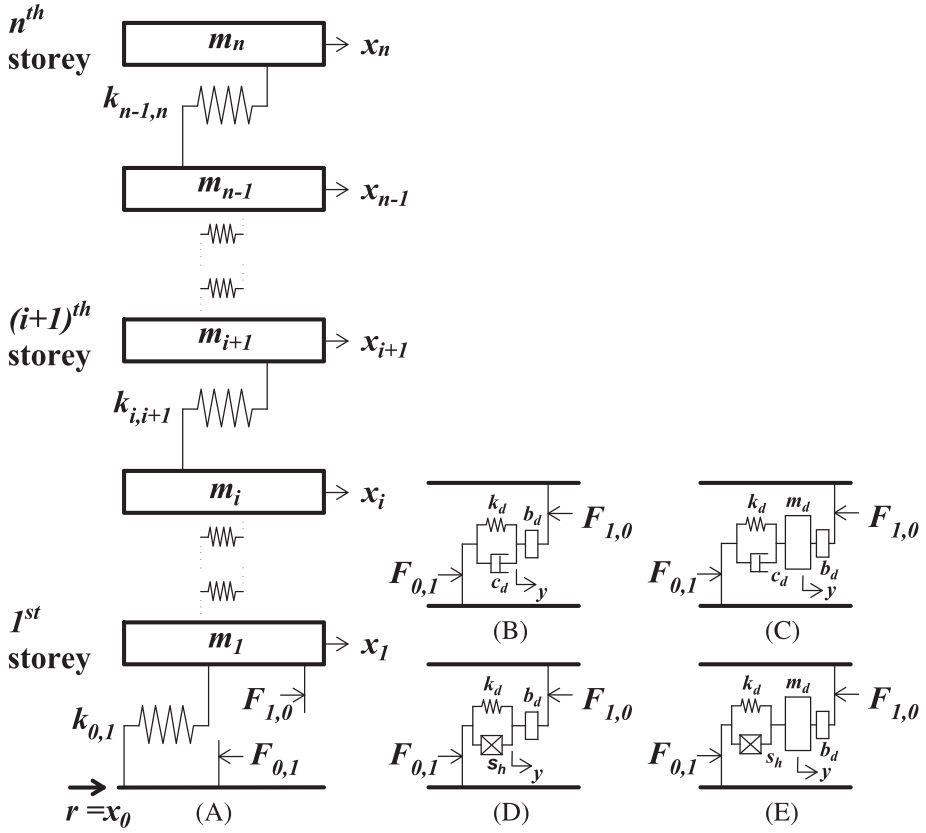

FIGURE 1 (A) n-DOF structure, (B) TID, (C) TMDI, (D) TIhD, (E) TMhDI

TABLE 1 Force transferred to the structure by the inerter damper in the Laplace domain

Device type:	$F_{1,0}$
TID	$\frac{b_d s^2(c_d s+k_d)}{b_d s^2+c_d s+k_d}(R-X_1)$
TMDI	$\frac{b_d s^2(c_d s+k_d)}{(m_d+b_d)s^2+c_d s+k_d}(R-X_1)-\frac{b_d s^2 m_d s^2}{(m_d+b_d)s^2+c_d s+k_d}X_1$
TIhD	$\frac{b_d s^2(k_d(1+j\eta))}{b_d s^2+k_d(1+j\eta)}(R-X_1)$
TMhDI	$\frac{b_d s^2(k_d(1+j\eta))}{(m_d+b_d)s^2+k_d(1+j\eta)}(R-X_1)-\frac{b_d s^2 m_d s^2}{(m_d+b_d)s^2+k_d(1+j\eta)}X_1$

where m_i and $k_{i-1,i}$, $i \in [1 : n]$ represent the mass and stiffness between storeys $i-1$ and i; X_i represents the Laplace transform of the ith storey displacement, when $i = 0$, then $X_0 = R$, which represents the Laplace transform of the base displacement; s represents the Laplace transform variable and $F_{1,0}$ represents the force transferred to the structure by the inerter damper in the Laplace domain given in Table 1. The inerter damper systems in Table 1 have the additional parameters b_d, m_d, k_d, c_d and η which are the device inertance, mass, stiffness, viscous damping and hysteretic damping loss factor, respectively, and $j = \sqrt{-1}$.

2.1 | Optimisation in SDOF structures

In this section, the tuning procedures to obtain the optimum parameters of the hysteretic inerter-based devices in an SDOF structure will be derived based initially on the traditional concept using viscous damping, which is in this case being replaced by complex stiffness term $k_d(1 + j\eta)$ representing the material damping. Here, k_d is the stiffness of the inerter dampers and η is the loss factor of the hysteretic damping element. It should be noted that this model is a noncausal model, which means it is physically not realisable. However, this model has been widely accepted in analysis[43] to accurately represent a class of nonlinear damping,[44] as well as the phenomena of energy dissipation in a variety of materials such as rubber and viscoelastic polymers.[45-48] As a result, there is a limitation that the model proposed in this work is currently only applicable to linear structures.

Although the equivalent viscous damping is often directly used to obtain the approximate equal response between viscous and hysteretic damping, in this study, we found that the result is different after the optimisation process. This

limitation has also been reported in Wong[49] for the hysteretic dynamic vibration absorber (HDVA). Therefore, it is important to derive a formulation for obtaining the optimum parameters of an inerter device with hysteretic damping.

2.1.1 | Optimisation of the TIhD

Consider now a TIhD attached to a 1-DOF structure as shown in Figure 1 for $n = 1$. The transfer function X/R can be derived analytically and written in the frequency domain as

$$\left|\left(\frac{X}{R}\right)\right| = \sqrt{\frac{[(1-\mu q^2)-\lambda\mu q^2]^2 + [\eta(1-\mu q^2)]^2}{[(1-(1+\mu)q^2)-\mu\lambda q^2(1-q^2)]^2 + [\eta(1-(1+\mu)q^2)]^2}}, \tag{4}$$

where η is the loss factor of the hysteretic damping, $\mu = b_d/m_1$ is the inertance-to-mass ratio, $q = \omega/\omega_n$ is the frequency ratio, $\lambda = k_{0,1}/k_d$ is the stiffness ratio, ω is the forcing frequency (assuming a sine wave input) and $\omega_n = \sqrt{k_{0,1}/m_1}$.

The approximate optimum parameters of the TIhD can be analytically obtained based on fixed-point theory via an algebraic solution. This technique has been derived by Hu et al.[16] for the TID optimisation. Following the same procedure, and by replacing the viscous damping ratio ζ with the loss factor η, one obtains the η optimum for the TIhD as

$$\eta_{opt} = \sqrt{\frac{\eta_P^2 + \eta_Q^2}{2}}. \tag{5}$$

η_P and η_Q are given by

$$\eta_{P.Q}^2 = \frac{A - BCD}{E}, \tag{6}$$

where

$$\begin{aligned}
A &= (2\mu(1-(1+\mu)q_{P.Q}^2)^2(\mu q_{P.Q}^2(\lambda_{opt}+1)-1)(\lambda_{opt}+1))\\
B &= (2(1-\mu q_{P.Q}^2)^2\\
C &= ((1-(1+\mu)q_{P.Q}^2 - \lambda_{opt}\mu q_{P.Q}^2(1-q_{P.Q}^2))\\
D &= (\lambda_{opt}\mu q_{P.Q}^2 - \lambda_{opt}\mu(1-q_{P.Q}^2) - \mu - 1)\\
E &= (2\mu(1-(1+\mu)q_{P.Q}^2)^2(1-\mu q_{P.Q}^2)) - (2(1-\mu q_{P.Q}^2)^2(1+\mu)(1-(1+\mu)q_{P.Q}^2))
\end{aligned}$$

The frequency ratio at the first two fixed-points P and Q are the solution of the following equation:

$$q^4 - \left(\frac{2}{\lambda_{opt}\mu}(1+\lambda_{opt}+\mu+\lambda_{opt}\mu) - q_R^2\right)q^2 + \frac{2}{\mu^2\lambda_{opt}q_R^2} = 0. \tag{7}$$

The optimum stiffness ratio (λ_{opt}) can be obtained by using either

$$\lambda_{opt} = \frac{2(1+\mu q_R^4(1+\mu) - q_R^2(1+2\mu))}{\mu q_R^4(\mu q_R^4 - 2q_R^2(1+\mu)+2)} \tag{8}$$

or

$$\lambda_{opt} = \frac{2(q_R^2(3\mu+2\mu^2+1) - 2(1+\mu))}{q_R^2(\mu q_R^2(1+2\mu) - 2(1+2\mu+2\mu^2))} \tag{9}$$

where q_R is the frequency ratio at the third fixed-point R given by

$$q_R^2 = \frac{3}{2} + \frac{1}{\mu} + \sqrt{\left(\frac{3}{2}+\frac{1}{\mu}\right)^2 - \frac{2}{\mu}}. \tag{10}$$

Figure 2A,B shows the difference between the optimised TID and TIhD using fixed-point theory. It can be seen that for viscous damping, Figure 2A, the underlying peaks of ζ_P and ζ_Q are quite low in amplitude, and therefore, the peaks of the combined optimal curve are very close to the fixed points P and Q. However, in the hysteretic damping case, the

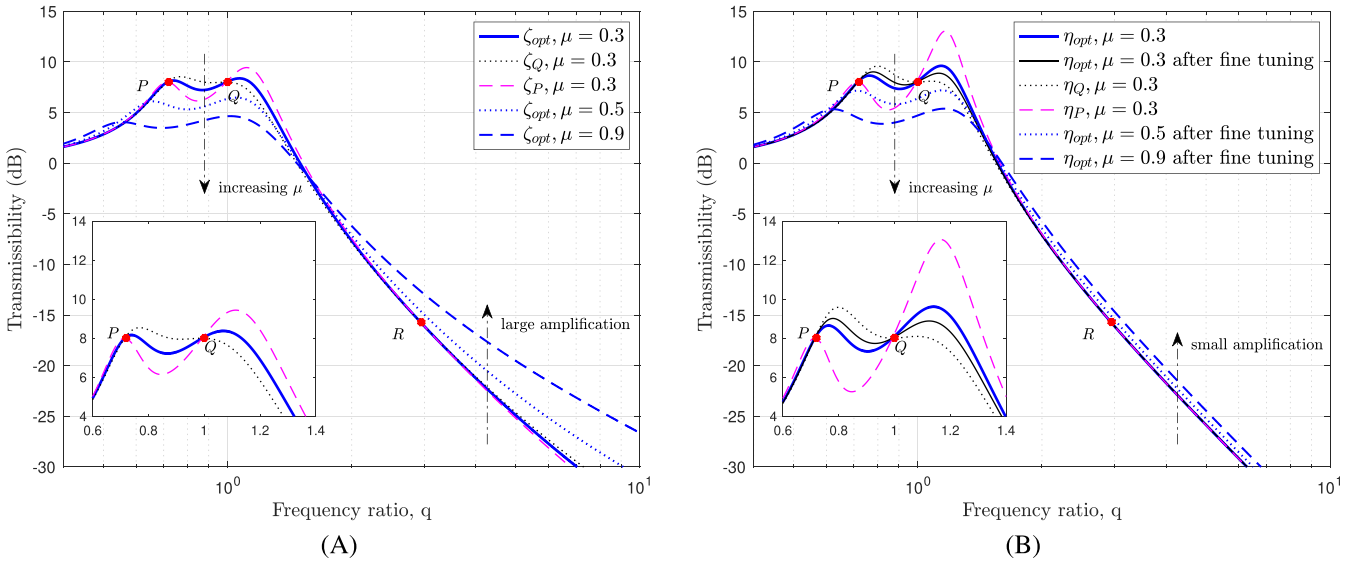

FIGURE 2 Transmissibility of a 1-DOF structure with (A) TID, (B) TIhD [Colour figure can be viewed at wileyonlinelibrary.com]

TABLE 2 Optimum damping ratio and loss factor of the inerter dampers

μ	ζ_{opt} of the TID	η_{opt} of the TIhD
0.3	0.0713	0.71
0.5	0.1264	0.92
0.9	0.2221	1.26

underlying peaks of η_P and η_Q are now quite high in amplitude, and therefore, the peaks of the combined optimal curve are much further away from the fixed points P and Q. It is therefore suggested that the optimised TIhD will require a further fine tuning process to make both peaks closer to equal amplitude. The effect of increasing μ is also obvious. It can be seen when μ is increased from 0.3 to 0.9, the TIhD shows a potential benefit in the higher frequency region where it has smaller amplification effect.

Table 2 presents the obtained optimum values of ζ and η after the optimisation process. As previously mentioned, equivalent viscous damping is often used to obtain an approximation for the response of a hysteretically damped system. However, this kind of approximation will not persist after the optimisation process. In this case, the equivalent viscous damping relationship $\eta = 2\zeta$ given in Chopra[37] cannot be used for the TIhD. The approximate relationship can instead be expressed as $\eta = 2\lambda\zeta$. It should be noted that this expression does not give the exact optimum solution—a point that was also noted by Wong[49] for the HDVA system. Therefore, it is important to derive the optimum η of the TIhD separately from the derivation of ζ of the TID.

2.1.2 | Optimisation of the TMhDI

TMhDI is basically a TIhD with a small secondary mass element m_d between the inerter b_d and the complex-stiffness element as illustrated in Figure 1C. The TMhDI model can potentially be used to represent an even more realistic device than the TIhD device. In this analysis, the inertance is designed to be dominant, where m_d is assumed to be just 5% of the inertance to represent the mass of the inertial device. Therefore, the tuning of the TMhDI follows the TIhD tuning rule based on fixed point analysis presented in the previous subsection.

Figure 3 shows the performance comparison in the frequency domain between the four considered inertial damper systems in an SDOF structure subjected to harmonic base displacement. Although the response at low frequencies is close for all four devices, it is clear from Figure 3A that the devices with hysteretic damping give significantly lower amplitude responses at higher frequencies. In this higher frequency range, the hysteretic damping also changes the phase angle as can be seen in Figure 3B.

2.2 | Optimisation in MDOF structures

First, we comment on the optimal location of the TMDI in MDOF structures. It is well known that the optimal location for a TMD is at the top of a MDOF structure and that the TID is optimum at the base of the structure.[14] The passive control

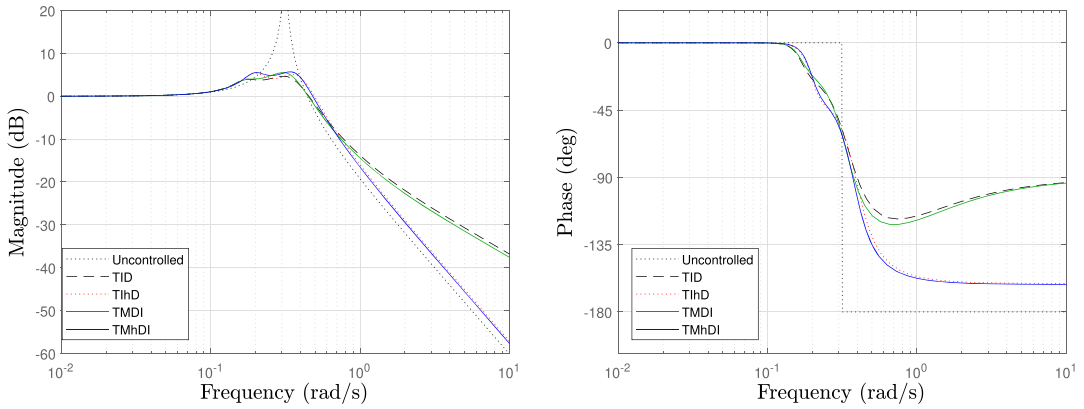

FIGURE 3 (A) Frequency response of a 1-DOF structure with optimised inertial damper systems. (B) Phase angle, $\mu = 0.9$ and $m_d = 5\%b_d$. High μ was chosen to clearly see the difference between the structural response with hysteretic and viscous damping above the resonance frequency [Colour figure can be viewed at wileyonlinelibrary.com]

forces in the Laplace domain can be written as follows when a TMDI is mounted at the ith storey level.

$$F_{i,i+1} = b_d s^2 (X_{i+1} - Y), \tag{11a}$$

$$F_{i+1,i} = (c_d s + k_d)(Y - X_i), \tag{11b}$$

where X_i represents the Laplace transform of the displacement of mass m_i and b_d is the inertance. The equation of motion for the y-DOF TMDI system can be written as

$$Y = \frac{b_d s^2 X_{i+1} + (c_d s + k_d) X_i}{(m_d + b_d)s^2 + c_d s + kd}. \tag{12}$$

Substituting Equation (12) into Equation (11a) gives

$$F_{i,i+1} = \frac{(b_d s^2 m_d s^2) X_{i+1} + b_d s^2 (c_d s + k_d)(X_{i+1} - X_i)}{(m_d + b_d)s^2 + c_d s + kd}, \tag{13a}$$

$$F_{i+1,i} = F_{i,i+1} = T_m X_{i+1} + T_d (X_{i+1} - X_i), \tag{13b}$$

where

$$T_d = \frac{b_d s^2 (c_d s + k_d)}{(m_d + b_d)s^2 + c_d s + k_d} \quad \text{and} \tag{14a}$$

$$T_m = \frac{b_d s^2 m_d s^2}{(m_d + b_d)s^2 + c_d s + k_d}. \tag{14b}$$

We now discuss the optimum placement of the TMDI in a n-DOF structure as shown in Figure 1. In matrix form, the equation of motion of the system can be written as

$$\mathbf{M}s^2 + \mathbf{K}Z = -\mathbf{M}\begin{bmatrix} 1 \\ 1 \\ \vdots \\ 1 \\ 1 \end{bmatrix} s^2 R + \begin{bmatrix} F_{1,0} - F_{1,2} \\ F_{2,1} - F_{2,3} \\ \vdots \\ F_{n-1,n-2} - F_{n-1,n} \\ F_{n,n-1} \end{bmatrix}, \tag{15}$$

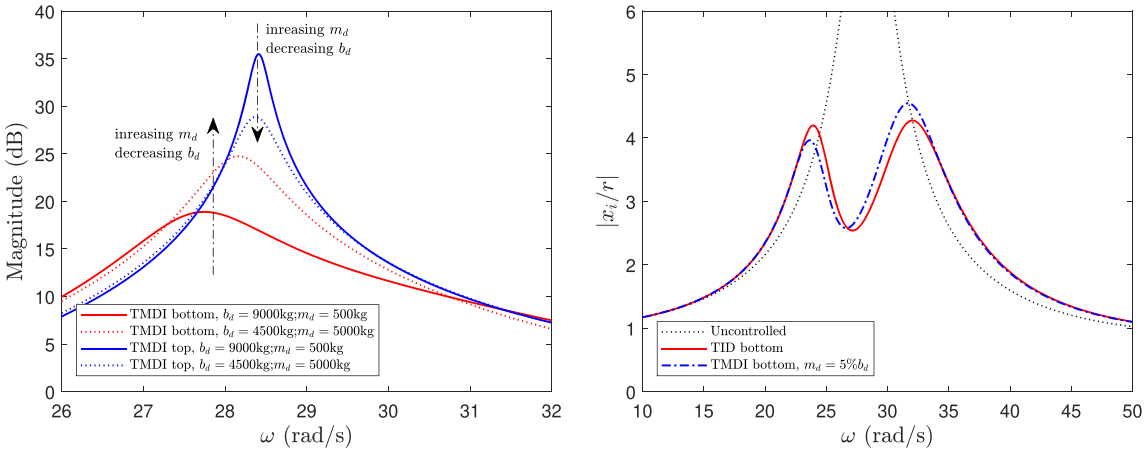

FIGURE 4 (A) The effect of increasing m_d to the TMDI optimum location. (B) Frequency response function (first mode) when $m_d = 5\%b_d$, $\mu = 0.62$ [Colour figure can be viewed at wileyonlinelibrary.com]

where $\mathbf{M}$ and $\mathbf{K}$ are the mass and stiffness matrices and $Z = X_i - R$ represents the vector of relative storey displacement. The above equation can also be written in form of modal matrices

$$\mathcal{M}s^2 + \mathcal{K}Z = -\Phi^T\mathbf{M}\begin{bmatrix}1\\1\\\vdots\\1\\1\end{bmatrix}s^2R + \Phi^T\begin{bmatrix}F_{1,0}-F_{1,2}\\F_{2,1}-F_{2,3}\\\vdots\\F_{n-1,n-2}-F_{n-1,n}\\F_{n,n-1}\end{bmatrix}, \tag{16}$$

where Φ is the eigenvector matrix and $\mathcal{M} = \Phi^T\mathbf{M}\Phi$ and $\mathcal{K} = \Phi^T\mathbf{K}\Phi$ are the modal mass and stiffness matrices, respectively.

Now, we consider the cases where the TMDI is mounted at either the bottom or top storey level. Assuming that only the first vibration mode is significant, the following transfer functions can be obtained:

TMDI at bottom storey level

$$\frac{Q_1}{R} = \frac{-\sum_{i=1}^{n}(m_1\Phi_{i,1})s^2 + \Phi_{1,1}T_m}{m_{m_1}s^2 + k_{m_1} + T_d\Phi_{1,1}^2}. \tag{17}$$

TMDI at top storey level

$$\frac{Q_1}{R} = \frac{-\sum_{i=1}^{n}(m_1\Phi_{i,1})s^2 + (\Phi_{n,1}-\Phi_{n-1,1})T_m}{m_{m_1}s^2 + k_{m_1} + T_d(\Phi_{n-1,1}-\Phi_{n,1})^2 - T_m\Phi_{n-1,1}(\Phi_{n,1}-\Phi_{n-1,1})}. \tag{18}$$

It is obvious that when the mass element of the TMDI is small or close to zero, the above equations will be identical to the TID transfer functions given in Lazar et al.[14]

Figure 4A shows how the optimum location of the TMDI changes between top and bottom story level by increasing m_d and decreasing b_d at the same time using Equations (17) and (18). It can be seen that increasing m_d will make the TMDI at the bottom story less effective. Conversely, decreasing m_d makes its performance better when placed on the bottom story. This aligns with our assumption of making the m_d only 5% of the device inertance, to represent the mass of the inerter device.

Furthermore, the optimum parameters of the TID in a MDOF structure were obtained by using a method proposed by Lazar et al.[14] Figures 2A,B and 4A have already demonstrated that the tuning procedure of the TID can be used for estimating the optimum parameters of the TIhD, TMDI and TMhDI. However, as previously noted, additional fine tuning is required to get the actual optimum values for these three systems, and this is also the case for MDOF systems.

2.3 | Concluding Remarks

From the discussion above, it can be concluded that when the damping in the tuned-inerter devices (TID and TMDI) exhibits linear hysteretic (TIhD and TMhDI) rather than viscous, the behaviour of the devices will be different, especially at the higher frequency of excitations. This is obvious from the frequency response analysis of the systems. However, obtaining the structural response in the time domain will be challenging due to the inherent occurrence of unstable poles. Hence, a robust time domain technique is required to capture the hysteretic behaviour rather than using an equivalent viscous damping method.

The following section will describe this new method for obtaining the time domain response of structures with linear hysteretic damping. Furthermore, some validations of the method are presented.

3 | TIME DOMAIN MODELLING

In this section, for the first time in the time domain analysis, the hysteretic-based inerter systems are evaluated by means of analytic signals and time reversal technique. The method used here is based on that proposed by Inaudi and Makris[41] in an extended and modified format that allows for the evaluation of the TIhD and TMhDI systems. The hysteretic damping is modelled in the form of a complex stiffness element of the inerter device. Hilbert functions are used to represent the analytic signals of the structural responses.

It should be noted that this time domain method does not change the noncausality of the linear hysteretic damping. It has been a long standing problem that complex stiffness model is a noncausal model and therefore very difficult to deal with. However, this model has been widely used[43] and has been proven to be very accurate and practical for modelling several engineering applications, for example, linearisation of nonlinear damping.[41] Reference to the causal linear hysteretic damping model can be found in Makris.[39] Furthermore, the causality of the inerter-based damper devices has been extensively discussed in Makris[50] and Makris (2018).[51] Specifically, in Makris,[50] the concept of inertoviscoelasticity is introduced. This is a form of model built from combinations of springs, inerters and viscous damping elements. These type of mechanical networks were discussed in detail in that paper and have been proven to be causal. In Makris,[51] the time-response function of three-element (spring, dashpot, inerter) networks with different arrangements were considered. The method was adopted from Makris[50] to ensure the causality of the mechanical systems in the time domain.

In this paper, the focus is not to resolve the noncausality of the linear hysteretic damping (complex stiffness) model, but to give a better representation of that model in the time domain in addition to the frequency domain. The time reversal technique is adopted and extended from Inaudi and Makris[41] to resolve the unstable poles from the differential equations. A new efficient numerical method is proposed, which is also applicable for MDOF systems and nonstationary input signals.

However, there are some important nuances to consider. Specifically, Bae et al.[52] showed that the Hilbert transform of the external impulse signal using the discrete Fourier transform (FT) and inverse Fourier transform (IFT) produces a totally different result compared with the one obtained from its exact formula. Not only this, Bae et al.[53] also showed that the Hilbert transform of a signal may produce a nonzero value at the beginning of the signal although its original real signal has zero value at time zero. To solve these problems, Bae et al.[52,53] introduced a technique called discrete convolution Hilbert transform (DCHT) and extended-time-duration using a Newton–Raphson iteration method. In the DCHT technique, the external amplitude of the force signal is divided into a finite number of rectangular signals. The Hilbert transform of the force signal can then be obtained from the Hilbert transform of each of the rectangular signals. The application of this method to a free and transient response of a hysteretic damping system was presented in Bae et al.[54,55] A system with hysteretic damping was studied in the case of triangular external force. A more complex system consisting of a mixed viscous-hysteretic damping was studied in Bae et al.[56] using this method.

However, unlike these previous methods that require some special integration techniques based on zero or first order hold methods, the modified method proposed in this paper makes it possible to solve the system in state space form using standard numerical integration algorithms, such as the Runga–Kutta family of solvers that are readily available within MATLAB. A detailed discussion about the method, in particular the time reversal technique, is presented next.

3.1 | Time reversal technique

In general, a continuous structural system can be observed by applying a discretisation process. Thus, the system can be simplified into a set of elements with a certain number of degrees of freedom (DOFs). The dynamic equation of motion

for an MDOF system can be expressed in matrix form as

$$\mathbf{M}\ddot{\mathbf{x}} + \mathbf{C}\dot{\mathbf{x}} + \mathbf{K}\mathbf{x} = \mathbf{F}. \tag{19}$$

The sizes of the matrices in Equation (19) are defined by the number of DOFs, n. The first and second derivatives with respect to the time are denoted by the dot, [$\dot{}$], and the double dots, [$\ddot{}$]. Here, $\mathbf{x}$ $(n \times 1)$ and $\mathbf{F}$ $(n \times 1)$, respectively, are the displacement and force vectors, whereas $\mathbf{M}$ $(n \times n)$, $\mathbf{C}$ $(n \times n)$ and $\mathbf{K}$ $(n \times n)$ represent the mass, damping and stiffness matrices.

The mass, stiffness and damping matrices are associated with the properties of the structure, that is, material weight, elasticity and damping coefficient. In particular, there are various ways to define the damping of the system, that is, viscous damping and hysteretic damping. The viscous damping force is represented in Equation (19) as the term $\mathbf{C}\dot{\mathbf{x}}$. However, in a linear hysteretic damping case, the damping force is a displacement-dependent term. It is usually modelled proportional to the complex value of the stiffness. Hence, Equation (19) becomes

$$\mathbf{M}\ddot{\mathbf{x}} + \mathbf{K}(1 + j\mathbf{G})\mathbf{x} = \mathbf{F}\,, \tag{20}$$

where $\mathbf{G}$ is the matrix of damping coefficient that represents the loss factor of each element of the system.

It is a common practice to avoid using complex coefficients for transient response or time-domain analysis, because in this case the damping model does not have a direct physical realisation. For this reason, the linear hysteretic damping is often represented by an equivalent viscous damping. Assuming constant amplitude oscillatory motion with a frequency ω, the two damping forces are identical if

$$\mathbf{G}\,\mathbf{K} = \mathbf{C}\,\omega. \tag{21}$$

Hence, an equivalent viscous damping can be selected for a particular frequency of interest as

$$\mathbf{C_{eq}} = \frac{1}{\omega}\,\mathbf{G}\,\mathbf{K}. \tag{22}$$

The selection of ω is typically the dominant frequency at which the damping is active, that is, the first natural frequency. However, in reality, the individual element damping occurs at different frequencies. Thus, accurate solutions can only be obtained if the excitation frequency is at or near the selected ω.

In the present work, it is essential to evaluate hysteretic damping in its original complex form to obtain an optimum design of TIhD and TMhDI. Moreover, the investigation of earthquake excitation force is one of the interests in the current work. Therefore, to address this issue, the time reversal technique of Inaudi and Makris[41] is adopted and modified.

Inaudi and Makris suggested that the displacements and the forces can be evaluated in analytic forms, that is, complex signals constructed by real and imaginary components. Hence,

$$\mathbf{x_a}(t) = \mathbf{x}(t) + j\,H[\mathbf{x}(t)], \tag{23}$$

$$\mathbf{F_a}(t) = \mathbf{F}(t) + j\,H[\mathbf{F}(t)], \tag{24}$$

where $H[]$ denotes the Hilbert transform of the original displacement and force functions. These analytic signals satisfy the boundary conditions of $x_a(-\infty) = x_a(\infty) = 0$ and $F_a(-\infty) = F_a(\infty) = 0$.

Therefore, in a state-space form, Equation (20) can be rewritten as

$$\dot{\mathbf{x}}_\mathbf{a}(t) = \mathbf{A}\,\mathbf{x_a}(t) + \mathbf{B}\,r_a(t), \tag{25}$$

where

$$\mathbf{x_a}(t) = \begin{bmatrix} \mathbf{x_a}(t) \\ \dot{\mathbf{x}}_\mathbf{a}(t) \end{bmatrix}, \qquad \mathbf{A} = \begin{bmatrix} \mathbf{0} & \mathbf{I} \\ -\mathbf{M^{-1}}\,\mathbf{K}(1 + j\mathbf{G}) & \mathbf{0} \end{bmatrix}, \qquad \mathbf{B} = \begin{bmatrix} \mathbf{0} \\ \mathbf{M^{-1}L_F} \end{bmatrix}, \qquad \mathbf{F_a}(t) = \mathbf{L_F}\,r_a(t). \tag{26}$$

It is important to note that the vectors and matrices denoted by x_a $(2n \times 1)$, $\mathbf{A}$ $(2n \times 2n)$, $\mathbf{B}$ $(2n \times 1)$ and L_F $(n \times 1)$ are all in complex form. The force vector in analytic form, F_a, is defined as the product of the complex time function, r_a, with a coefficient vector of elements' load factor, L_F, whereas $\mathbf{0}$ $(n \times 1)$ and $\mathbf{I}$ $(n \times 1)$ are the zeros and identity matrices, respectively.

Despite seeming that Equation (25) can be solved directly involving a standard integration procedure, that is, convolution integral, the eigenvalues of $\mathbf{A}$ are pairs of stable and unstable roots.[41] Therefore, a special treatment is required to obtain the stable solutions of Equation (25). Inaudi and Makris[41] introduced a backward integration technique that reverses the independent variable (time) in the modal coordinate of the unstable parts. The analytic vector x_a can be rewritten by defining analytic modal coordinates, $\mathbf{q}_{\mathbf{k}_a}$ and $\mathbf{q}_{\mathbf{l}_a}$, for the stable and unstable parts, respectively.

$$\mathbf{x}_\mathbf{a}(t) = \Phi \begin{bmatrix} \mathbf{q}_{\mathbf{k}_a}(t) \\ \mathbf{q}_{\mathbf{l}_a}(t) \end{bmatrix}, \tag{27}$$

where $\mathbf{q}_{\mathbf{k}_a} = \mathbf{q}_\mathbf{k} + j\ H[\mathbf{q}_\mathbf{k}]$ and $\mathbf{q}_{\mathbf{l}_a} = \mathbf{q}_\mathbf{l} + j\ H[\mathbf{q}_\mathbf{l}]$, whereas $\boldsymbol{\Phi}$ $(2n \times 2n)$ is the eigenvector matrix of $\mathbf{A}$.
By introducing a reversed time, $z = -t$, and a function $\tilde{\mathbf{q}}_\mathbf{l}(z) = \mathbf{q}_\mathbf{l}(t)$, hence,

$$\dot{\mathbf{q}}_\mathbf{l}(t) = -\tilde{\mathbf{q}}'_\mathbf{l}(z), \tag{28}$$

where $[']$ defines the derivative in the reversed time. Therefore, Equation (25) can be rewritten as

$$\begin{bmatrix} \dot{\mathbf{q}}_{\mathbf{k}_a}(t) \\ -\tilde{\mathbf{q}}'_{\mathbf{l}_a}(z) \end{bmatrix} = \mathbf{A}^* \begin{bmatrix} \mathbf{q}_{\mathbf{k}_a}(t) \\ \tilde{\mathbf{q}}_{\mathbf{l}_a}(z) \end{bmatrix} + \mathbf{B}^* \begin{bmatrix} r_a(t) \\ \tilde{r}_a(z) \end{bmatrix}, \tag{29}$$

where $\mathbf{A}^* = \boldsymbol{\Phi}^{-1}\mathbf{A}\boldsymbol{\Phi}$ and $\mathbf{B}^* = \boldsymbol{\Phi}^{-1}\mathbf{B}$. To be noted here, $\mathbf{A}^*$ is a diagonal matrix; thus, Equation (29) becomes uncoupled. Hence, components of $\mathbf{q}_{\mathbf{k}_a}$ and $\mathbf{q}_{\mathbf{l}_a}$ can be evaluated separately by means of forward time integration and backward time integration, respectively.

Inaudi and Makris[41] numerically solved both a SDOF problem and a 2-DOF problem by applying discrete-time sampling to the analytical integral solutions of Equation (29). However, this approach may be difficult to implement in a more complex and higher DOFs system as it requires the analytical integral solution for each different system. Therefore, in the present work, a more robust computational approach is proposed. Herein, a variable separation procedure is applied to separate the real and imaginary components in Equation (29); hence,

$$\begin{bmatrix} \dot{\mathbf{q}}_\mathbf{k}(t) \\ H[\dot{\mathbf{q}}_\mathbf{k}(t)] \\ -\tilde{\mathbf{q}}'_{\mathbf{l}_a}(z) \\ -H[\tilde{\mathbf{q}}'_{\mathbf{l}_a}(z)] \end{bmatrix} = \begin{bmatrix} \mathbf{A}^{**} & \mathbf{0} \\ \mathbf{0} & \tilde{\mathrm{A}}^{**} \end{bmatrix} \begin{bmatrix} \mathbf{q}_{\mathbf{k}_a}(t) \\ H[\mathbf{q}_{\mathbf{k}_a}(t)] \\ \tilde{\mathbf{q}}_{\mathbf{l}_a}(z) \\ H[\tilde{\mathbf{q}}_{\mathbf{l}_a}(z)] \end{bmatrix} + \begin{bmatrix} \mathbf{B}^{**} \\ \tilde{\mathbf{B}}^{**} \end{bmatrix} \begin{bmatrix} r_a(t) \\ \tilde{r}_a(z) \end{bmatrix}, \tag{30}$$

which can be evaluated separately for forward integration

$$\begin{bmatrix} \dot{\mathbf{q}}_\mathbf{k}(t) \\ H[\dot{\mathbf{q}}_\mathbf{k}(t)] \end{bmatrix} = \mathbf{A}^{**} \begin{bmatrix} \mathbf{q}_{\mathbf{k}_a}(t) \\ H[\mathbf{q}_{\mathbf{k}_a}(t)] \end{bmatrix} + \mathbf{B}^{**} r_a(t) \tag{31}$$

and backward integration

$$\begin{bmatrix} -\tilde{\mathbf{q}}'_{\mathbf{l}_a}(z) \\ -H[\tilde{\mathbf{q}}'_{\mathbf{l}_a}(z)] \end{bmatrix} = \tilde{\mathrm{A}}^{**} \begin{bmatrix} \tilde{\mathbf{q}}_{\mathbf{l}_a}(z) \\ H[\tilde{\mathbf{q}}_{\mathbf{l}_a}(z)] \end{bmatrix} + \tilde{\mathbf{B}}^{**} \tilde{r}_a(z). \tag{32}$$

In Equations (31) and (32), the matrices $\mathbf{A}^{**}$ $(2n \times 2n)$, $\tilde{\mathrm{A}}^{**}$ $(2n \times 2n)$, $\mathbf{B}^{**}$ $(2n \times 1)$ and $\tilde{\mathbf{B}}^{**}$ $(2n \times 1)$ consisted of components that provide coupling between the real and imaginary parts of each modal coordinate.

The key aspect in the present work is that Equations (31) and (32) are sets of ordinary differential equations (ODEs); thus, they can be straightforwardly solved via a standard numerical procedure, that is, by using the Runge–Kutta method. Therefore, it provides a more robust approach to evaluate any structural system as long as the mass, stiffness, damping matrices and the force vector are known. Further discussion on the computational algorithm of the present approach is given in Appendix B1.

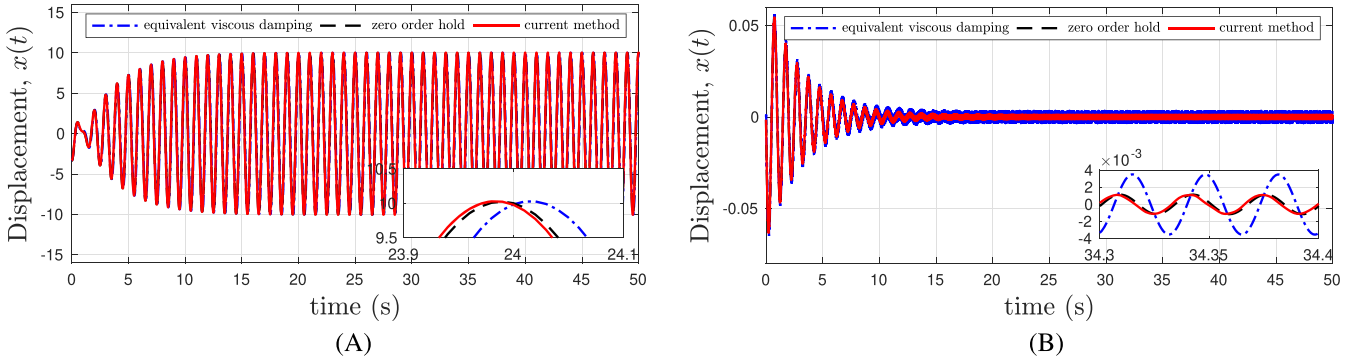

FIGURE 5 Time history responses of SDOF structure (A) $\omega = \omega_n$, (B) $\omega = 30\omega_n$ subjected to sine-wave ground displacement with amplitude $R = 1$ unit length [Colour figure can be viewed at wileyonlinelibrary.com]

TABLE 3 Optimum parameters of the inertial damper systems

	SDOF structure, $\mu = 0.1$				3-DOF structure, $\mu = 0.18$			
Parameters	**TID**	**TMDI**	**TIhD**	**TMhDI**	**TID**	**TMDI**	**TIhD**	**TMhDI**
Inertance, $b_d(kNs^2/m)$	0.1	0.1	0.1	0.1	0.48	0.48	0.48	0.48
Stiffness, $k_d(kN/m)$	0.0085	0.0091	0.0085	0.0091	138.6	146	138.6	146
Viscous damping, $c_d(kNs/m)$	0.0107	0.0107	–	–	2.5	2.5	–	–
Loss factor, η	–	–	0.3848	0.3848	–	–	0.3060	0.2905
Secondary mass, $m_d(kNs^2/m)$	–	0.005	–	0.005	–	0.024	–	0.024

3.2 | Validation

In this subsection, validations of the new computational approach are presented. An example of a SDOF system excited by a harmonic sine-wave input is now considered. The results of the present computational approach are compared with those obtained via the zero-order hold method of Inaudi and Makris.[41]

Figure 5A,B shows the time domain response of a simple SDOF system with one mass and one coupled spring-damping element represented by a complex stiffness subjected to sinewave ground displacement. It is obvious that the solution using the present method are in a good agreement with the zero-order hold method by Inaudi and Makris[41] around the resonance ($\omega = \omega_n$) and away from resonance ($\omega = 30\omega_n$). Here, ω is the frequency of excitation and ω_n is the natural frequency of the system. In addition, a comparison with a common method using equivalent viscous damping is also presented when the equivalency is made at the resonance. As can be seen in Figure 5B, the equivalent viscous damping method becomes inaccurate at frequencies away from the natural frequency.

The following section will discuss further case studies where the time reversal method is applied for analysis of structures with TIhD and TMhDI.

4 | CASE STUDIES

4.1 | Harmonic base excitation

An SDOF structure as shown in Figure 1A for $n = 1$, mass m and stiffness $k_{0,1}$ set to $1kNs^2/m$ and $0.0987kN/m$, respectively was used in this example. Figure 6A shows the performance comparison between the four inerter-based damper systems applied to an SDOF structure. Their optimised parameters are given in Table 3. It can be seen from this figure that the performance of the TID and the TMDI is similar. This can be understood because the effect of m_d, which is only 5% of the inertance, is small across the frequencies. However, the TMDI has slightly higher response around the resonant frequency after the optimisation. Its time domain response is given in Figure 7A,B obtained by using the method presented in the previous section. A similar result also can be seen for the TIhD compared with the TMhDI, which indicates that the effect of m_d is very small.

Although the response amplitude around the resonant frequency is slightly higher with the hysteretic damping, it has a potential benefit in the higher frequency region as previously discussed. The attenuation difference between TID/TMDI and TIhD/TMhDI in the high frequency region is 20 dB/dec. In civil engineering applications, especially for low frequency

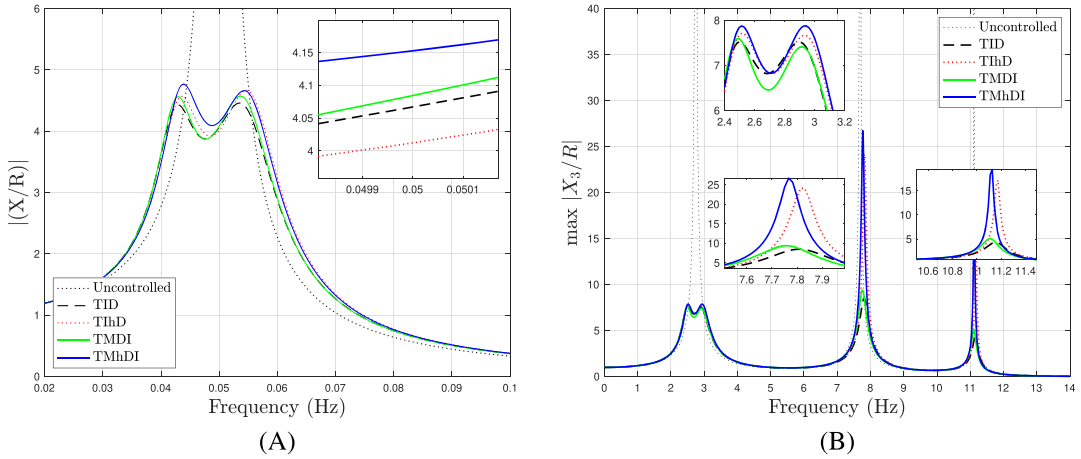

FIGURE 6 Transmissibility of (A) SDOF structure, $\mu = 0.1$, (B) 3-DOF structure, $\mu = 0.18$ [Colour figure can be viewed at wileyonlinelibrary.com]

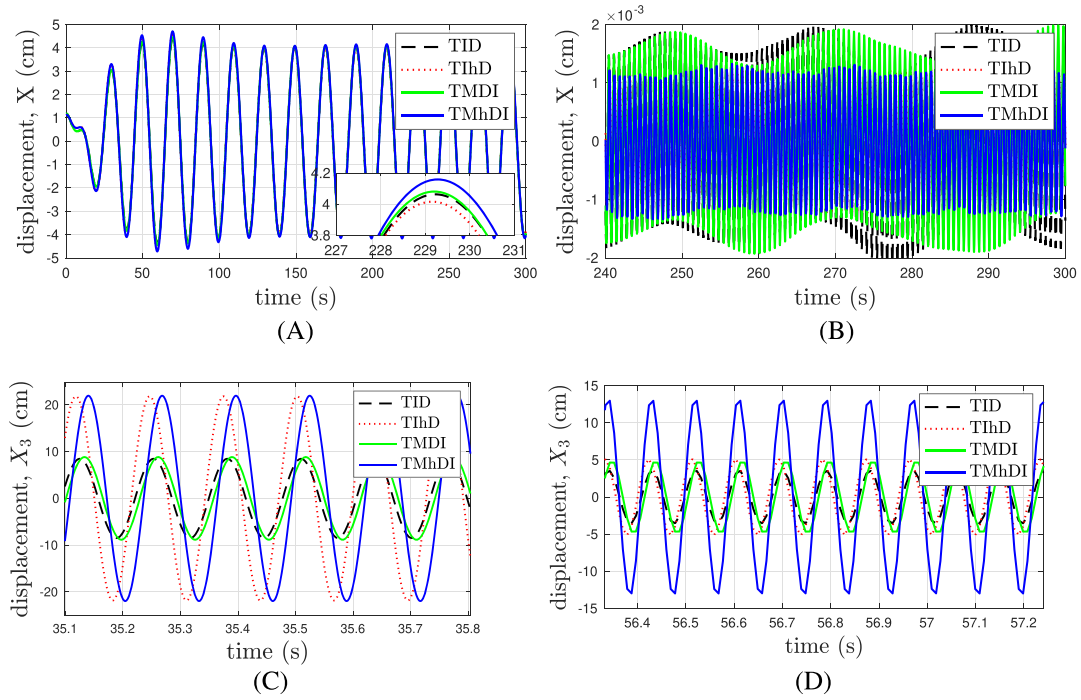

FIGURE 7 Time history responses at steady state of SDOF structure, $\mu = 0.1$, $\omega = 0.05$ Hz (A) and $\omega = 30\omega_n$ (B) and 3-DOF structure, $\mu = 0.18$, $\omega = 7.8$ Hz (C), and ω= 11.1 Hz (D) subjected to sine wave ground displacement with amplitude $R = 1$ cm [Colour figure can be viewed at wileyonlinelibrary.com]

structures such as base-isolated structures, this is a valuable benefit because the response around the resonance frequency needs to be reduced to deal with long-period earthquakes, while at the same time maintaining lower response at the higher frequency region.

To explore MDOF structures, a 3-DOF structure as shown in Figure 1A for $n = 3$ was selected for a case study. The parameters of the structure were designed to be the same with the 3-DOF structure presented in Lazar et al.,[14] where $m_1 = m_2 = m_3 = 1kNs^2/m$ and $k_{0,1} = k_{1,2} = k_{2,3} = 1500kN/m$. All of the inerter-damper devices shown in Figure 1B – D were located at the bottom storey as this is their optimum location.

Figure 6B shows the transfer function X_3/R of a 3-DOF structure in the frequency domain. Its time domain response is given in Figure 7C,D. The optimised parameters of the inerter-damper devices are given in Table 3 derived based on a fixed value of $\mu = 0.18$. The structural response amplitude around the first resonance frequency is similar for all cases. As mentioned previously for SDOF structures, the hysteretic damping gives a slightly higher response after the

optimisation. However, around the second and third resonance frequencies, the response of the structure with TIhD and TMhDI is significantly higher when compared with the TID and TMDI with no hysteretic damping. This is because the force transferred to the structure by the TIhD and the TMhDI is larger than that of TID and TMDI. This also indicates that modelling a system that has hysteretic damping with a viscous damping model may significantly overestimate the level of damping that can be achieved in higher modes of vibration. As a result, using the model proposed in this paper may have considerable benefits for modelling physical systems of this type.

4.2 | Earthquake base excitation

A further benefit of the proposed time domain method for linear hysteretic damping is its ability to be used for nonsinusoidal and nonperiodic forcing functions such as earthquakes. The fixed-point theory (FPT) approach discussed in the previous section assumes a harmonic input signal, which is not directly applicable to seismic applications where the excitations are not harmonic in nature. Therefore, in this study, a numerical optimisation approach using the Self-Adaptive Differential Evolution algorithm (SADE)[57] is adopted and MATLAB is employed to apply the algorithm. The SADE algorithm is an improved differential evolution (DE) algorithm[58] that is capable of adaptively choosing the learning strategy to obtain a global optimum solution of the defined objective function. In this algorithm, a parameter candidate pool is generated for each generation. The number of generations was defined based on at which the result was converged. The detailed procedure of the SADE algorithm can be found in Qin and Suganthan.[57]

The four tuned-inerter devices were optimised for an SDOF structure as shown in Figure 1A for $n = 1$. Mass m and stiffness $k_{0,1}$ were assumed to be $1kNs^2/m$ and $1kN/m$, respectively. The objective chosen was to find the optimum values of b_d, k_d and c_d or η that gives minimum average root-mean-square (RMS) value of the top displacement response for all considered earthquakes. This condition can be expressed as

$$min \left| \frac{\sum_{\ell=1}^{N_e} \mathrm{RMS}(x_\ell(t))}{N_e} \right|, \tag{33}$$

where N_e is the number of earthquake input signals considered. Note that the upper and lower limits of the parameter values for inertance, stiffness and damping must be set to realistic values. In this study, the limits are selected to be $0.1 \leq b_d \leq 0.9; 0.1 \leq k_d \leq 1; 0.1 \leq \eta \leq 2$; and $0.1 \leq c_d \leq 3$.

Three design response spectrum were selected: (1) Arrete 2010–2011, representing high-frequency earthquakes; (2) NTC2004 - a, representing low-frequency earthquakes; and (3) NTC2004 - b, representing mid-frequency earthquakes. The following assumptions were made: (1) for Arrete 2010–2011: seismic zone 1; ground type A; and building class 3, (2) for NTC2004 - a: ground type IIIc, for (3) NTC2004 - b: ground type II. Ten artificial earthquakes were generated using the SeismoArtif software for each of the corresponding design spectra as shown in Figure 8. Earthquakes 1–10 correspond to Arrete 2010–2011, Earthquakes 11–20 correspond to NTC2004 - a, and Earthquakes 21–30 correspond to NTC2004 - b. This enabled the effect of the hysteretic damping and the small mass element m_d, which was assumed to be 5% of the inertance b_d to be observed. In order to try and make meaningful comparisons, the results are presented in terms of normalised RMS of the seismic displacement response histories of the structural system.

The optimum parameters obtained for the devices using the SADE algorithm and FPT are given in Table 4. As can be seen from this table, there is no obvious correlation between the optimum η of the TIhD and TMhDI with the optimum c_d of the TID and TMDI. This implies that equivalent viscous damping cannot be used, because each of the devices needs to be individually optimised.

Figure 9 shows the performance comparison between the SADE and FPT optimisations. Each bar in the figure represents the difference between FPT and SADE for each device for that specific earthquake with FPT taken as 0% for the sake of comparison. If no bar is shown, then there is a negligible difference between FPT and SADE. As would be expected, almost all of the bars for SADE are below the FPT line. The average is −3.64% for Case (1) Arrete 2010–2011 (high-frequency) Earthquakes 1–10, −44.38% for Case (2) NTC2004 - a (low-frequency) Earthquakes 11–20, and −10.42% for Case (3) NTC2004 - b (mid-frequency) Earthquakes 21–30. It should be noted that the natural frequency of the considered SDOF structure is 0.16 Hz, which is in this case in the range of the low-frequency earthquakes.

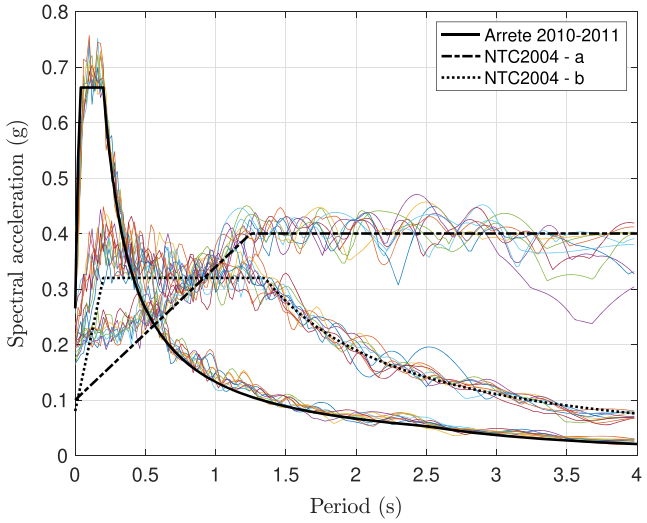

FIGURE 8 Design response spectrums and 30 generated artificial earthquakes [Colour figure can be viewed at wileyonlinelibrary.com]

	Fixed-point theory				SADE algorithm			
Parameters	**TID**	**TMDI**	**TIhD**	**TMhDI**	**TID**	**TMDI**	**TIhD**	**TMhDI**
Inertance, $b_d(kNs^2/m)$	0.9	0.9	0.9	0.9	0.9	0.9	0.9	0.9
Stiffness, $k_d(kN/m)$	0.38	0.43	0.35	0.36	0.85	0.88	0.91	0.89
Viscous damping, $c_d(kNs/m)$	0.44	0.44	–	–	1.64	1.74	–	–
Loss factor, η	–	–	1.26	1.26	–	–	1.73	1.83
Secondary mass, $m_d(kNs^2/m)$	–	0.045	–	0.045	–	0.045	–	0.045

TABLE 4 Optimum parameters of the inertial damper systems for an SDOF structure

Note. The optimum parameters obtained by the SADE algorithm for each of the device in the table are based on the objective function given in Equation (33).

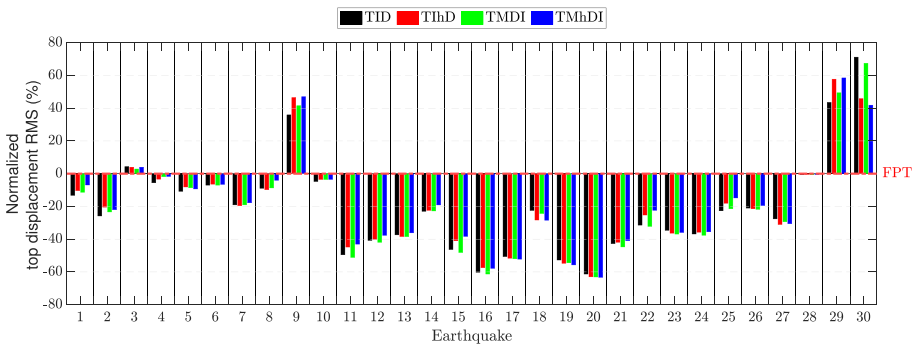

FIGURE 9 Performance comparison between the SADE and FPT optimisations. Any bars that are very close to the FPT values are not shown and can be assumed to be approximately the same as the FPT value. Earthquakes 1 to 10 correspond to Case (1): Arrete 2010–2011, earthquakes 11 to 20 correspond to Case (2): NTC2004 - a, and earthquakes 21 to 30 correspond to Case (3) NTC2004 - b [Colour figure can be viewed at wileyonlinelibrary.com]

From Figure 9, it can be observed that overall the optimisation by SADE algorithm works better than the FPT, particularly for low-frequency earthquakes (Earthquakes 11–20). For Earthquakes 9, 29 and 30, the FPT is actually better than SADE. It is not clear what the reason for this is, but one possible explanation is that the objective function given in Equation (33) is designed to seek for the minimum overall average, not the minimum for each of the earthquakes. Overall, the average is −24.66% for the bars below FPT and 5.18% for the bars above the FPT. This means that the optimisation using the SADE algorithm gives a much better response compared with the FPT across all 30 earthquake cases. In terms of applications, computations of this type can be used during the design stage, in order to give estimates of the level of displacement responses in a structure where the damping in the inerter device is hysteretic.

Figure 10 shows a comparison of the performance of the four devices for each earthquake, for the three different cases considered. Each of the device was optimised by using the SADE algorithm. The comparison was made relative to the TID performance, which was the best overall. So in this figure, each bar represents the difference between each device and TID (which is taken as 0%) for each earthquake.

An example of the time domain response is given in Figure 11 for both SADE and FPT optimisations. The trends observed in both Figures 9 and 10 can also be observed in these time domain plots. Specifically, the overall amplitudes

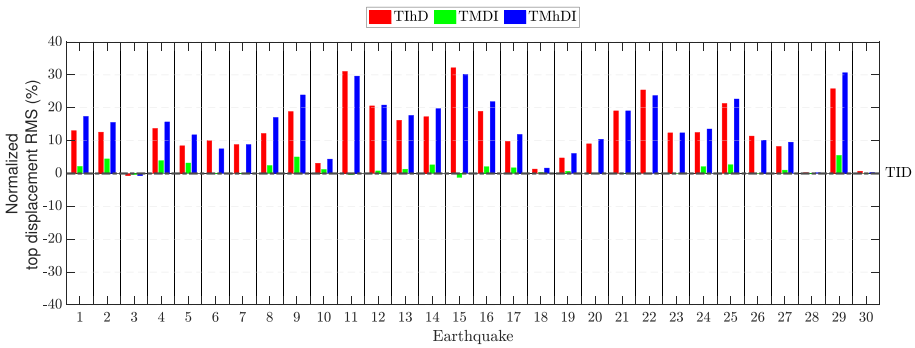

FIGURE 10 Performance comparison between the four devices. Any bars that are very close to the TID values are not shown and can be assumed to be approximately the same as the TID value. Earthquakes 1 to 10 correspond to Case (1): Arrete 2010–2011, earthquakes 11 to 20 correspond to Case (2): NTC2004 - a, and earthquakes 21 to 30 correspond to Case (3) NTC2004 - b [Colour figure can be viewed at wileyonlinelibrary.com]

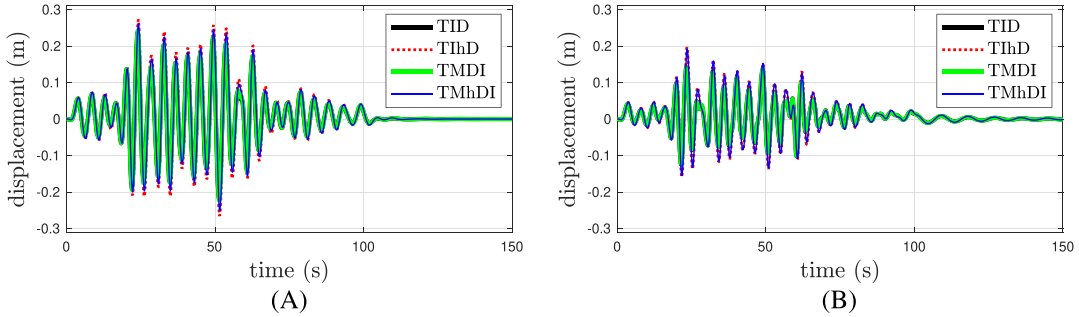

FIGURE 11 Time history responses of the structure subjected to Earthquake 15 base motion optimised by (A) FPT, (B) SADE [Colour figure can be viewed at wileyonlinelibrary.com]

in Figure 11B for SADE are significantly less that the amplitudes in Figure 11A for FPT. It is also possible to see that the hysteretic damping devices have higher amplitude responses than the TID or TMDI in both plots.

From Figures 10, we can infer that the effect of the secondary mass m_d is small due to the fact that the TMDI performance is only up to 6% different to the TID performance. The effect of the hysteretic damping was much larger, because the TIhD and TMhDI were up to 33% different to the TID results. This implies that when the physical damping behaviour in an inerter-based device is hysteretic, then the viscous damping approximation could lead to results that overestimate the effectiveness of the device.

The methodology presented in this paper offers an alternative modelling approach that can capture the effect of the hysteretic damping in the inerter-based device for arbitrary input signals such as earthquakes. As a result, it should be possible to obtain more accurate estimates of the device performance during a design procedure.

5 | CONCLUSIONS

This paper has introduced two novel passive inerter-based dampers, namely, the TIhD and TMhDI. Both devices were based on the well-established idealised concepts of the TID and TMDI with the viscous damping element being replaced by hysteretic damping element. The primary motivation was in order to create models that were able to capture the physical behaviour of structural systems in a more realistic way.

Among all the devices considered, the TMhDI is believed to be potentially the most realistic because it has both hysteretic damping and a small secondary mass, which captures the effect of the mass of the inerter device itself. It has been shown how the optimum parameters of both devices can be obtained via fixed-point theory although one limitation is that additional fine tuning is required for the devices with hysteretic damping. In addition, it was shown that there are regions of the frequency domain where the hysteretic damping leads to different transmissibility values compared to viscous damping. This was observed for both the SDOF and MDOF examples considered. For example, for the SDOF structure with harmonic excitation, both TIhD and TMhDI have the potential benefit of reducing displacement response in the higher frequency region, and the attenuation difference is of the order of 20 dB/dec. However, in the MDOF example, both hysteretic devices exhibit significantly higher amplitudes of displacement response for the higher modes of vibration

compared with the viscous damping model. This is something to be aware of in systems where the physical behaviour is closer to hysteretic than viscous.

For the earthquake signals considered here, the SADE algorithm was used to optimise the devices' parameters, and it was shown that the effect of additional small m_d, in this case is 5%, is not significant for the example considered. The TIhD and the TMhDI performance were shown to have a larger response than the TID and TMDI in the earthquake example. Moreover, the obtained optimum stiffness and damping parameters of the TIhD and TMhDI for the example considered do not satisfy the standard equivalent viscous damping relationship that would enable a conversion from the TIhD to TID or from TMhDI to TMDI. This implies that the TIhD and the TMhDI are better treated without using and equivalent viscous damping assumption when performing seismic design analysis.

This study has been made possible by first developing a time domain method via time reversal technique for the analysis of structural systems with linear hysteretic damping. The TIhD and TMhDI models subsequently developed offer an approach that can capture the systems' performance in a more realistic way when the physical behaviour of the system is closer to hysteretic than viscous. The method has also been validated by comparing the results with the zero-order hold method of Inaudi and Makris and with equivalent viscous damping. Future work will include verification of the method using experimental test results.

ACKNOWLEDGEMENT

The first and fourth authors would like to acknowledge the support from Indonesia Endowment Fund for Education (LPDP).

ORCID

Predaricka Deastra https://orcid.org/0000-0002-1709-4686

REFERENCES

1. Okumura A. Japan Patent Koukai. H09-177875; 1997.
2. Ikago K, Saito K, Inoue N. Seismic control of single-degree-of-freedom structure using tuned viscous mass damper. *Earthq Eng Struct Dyn*. 2012;41(3):453-474.
3. Swift S, Smith M, Glover A, Papageorgiou C, Gartner B, Houghton N. Design and modelling of a fluid inerter. *Int J Contr*. 2013;86(11):2035-2051.
4. Smith M. Synthesis of mechanical networks: the inerter. *IEEE Trans Autom Control*. 2002;47(10):1648-1662.
5. Papageorgiou C, Smith MC. Laboratory experimental testing of inerters. In: 44th IEEE Conference on Decision and Control and, European Control Conference, Vol. 2005; 2005:3351-3356.
6. Wang F, Hong M, Designing L. Designing and testing a hydraulic inerter. *Proc IME C J Mech Eng Sci*. 2011;225(1):66-72.
7. Saitoh M. On the performance of gyro-mass devices for displacement mitigation in base isolation systems. *Struct Control Health Monit*. 2012;19(2):246-259.
8. Ikago K, Sugimura Y, Saito K, Inoue N. Modal response characteristics of a multiple-degree-of-freedom structure incorporated with tuned viscous mass dampers. *J Asian Arch Build Eng*. 2012;11(2):375-382.
9. Liu X, Jiang J, Titurus B, Harrison A. Model identification methodology for fluid-based inerters. *Mech Syst Signal Process*. 2018;106:479-494.
10. Sugimura Y, Goto W, Tanizawa H, Saito K, Nimomiya T. *Response Control Effect of Steel Building Structure Using Tuned Viscous Mass Damper*, *Proceedings of the 15th World Conference on Earthquake Engineering*. Lisbon, Portugal; 2012;24-28.
11. Pan C, Zhang R, Luo H, Li C, Shen H. Demand-based optimal design of oscillator with parallel-layout viscous inerter damper. *Mech Syst Signal Process*. 2017;25(1):e2051.
12. Deastra P, Wagg D, Sims N. The realisation of an inerter-based system using fluid inerter. *Dynamics of Civil Structures*; 2019:127-134.
13. Tipuric M, Deastra P, Wagg D, Sims ND. Semi-active inerters using magnetorheological fluid: a feasibility study. Active and Passive Smart Structures and Integrated Systems XII. International Society for Optics and Photonics; 2018.
14. Lazar I, Neild S, Wagg D. Using an inerter-based device for structural vibration suppression. *Earthq Eng Struct Dyn*. 2014;43(8):1129-1147.
15. Den Hartog J. *Mechanical Vibrations*. York, PA USA: McGraw Hill; 1940.
16. Hu Y, Chen M, Shu Z, Huang L. Analysis and optimisation for inerter-based isolators via fixed-point theory and algebraic solution. *J Sound Vib*. 2015;346:17-36.
17. Lazar I, Neild S, Wagg D. Vibration suppression of cables using tuned inerter dampers. *Eng Struct*. 2016;122:62-71.
18. De Domenico D, Impollonia N, Ricciardi G. Soil-dependent optimum design of a new passive vibration control system combining seismic base isolation with tuned inerter damper. *Soil Dyn Earthq Eng*. 2018;105:37-53.
19. Deastra P, Wagg D, Sims N. The effect of a tuned-inerter-damper on the seismic response of base-isolated structures. In: Proceedings of the 16th European Conference On Earthquake Engineering Thessaloniki; 2018; Greece:18-21.

20. Marian L, Giaralis A. Optimal design of a novel tuned mass-damper-inerter (TMDI) passive vibration control configuration for stochastically support-excited structural systems. *Probab Eng Mech*. 2014;38:156-164.
21. Brzeski P, Kapitaniak T, Perlikowski P. Novel type of tuned mass damper with inerter which enables changes of inertance. *J Sound Vib*. 2015;349:56-66.
22. Pietrosanti D, De Angelis M, Basili M. Optimal design and performance evaluation of systems with tuned mass damper inerter (TMDI). *Earthq Eng Struct Dyn*. 2017;46(8):1367-1388.
23. Hashimoto T, Fujita K, Tsuji M, Takewaki I. Innovative base-isolated building with large mass-ratio TMD at basement for greater earthquake resilience. *Future Cities Env*. 2015;1(1):9.
24. De Domenico D, Ricciardi G. An enhanced base isolation system equipped with optimal tuned mass damper inerter (TMDI). *Earthq Eng Struct Dyn*. 2018;47(5):1169-1192.
25. Brzeski P, Lazarek M, Perlikowski P. Experimental study of the novel tuned mass damper with inerter which enables changes of inertance. *J Sound Vib*. 2017;404:47-57.
26. Hessabi R, Mercan O. Investigations of the application of gyro-mass dampers with various types of supplemental dampers for vibration control of building structures. *Eng Struct*. 2016;126:174-186.
27. Hessabi RM. *Application of Real-time Hybrid Simulation Method in Experimental Identification of Gyromass Dampers*. Toronto, Canada: Department of Civil Engineering, University of Toronto; 2017.
28. Gonzalez-Buelga A, Lazar I, Jiang J, Neild S, Inman D. Assessing the effect of nonlinearities on the performance of a tuned inerter damper. *Struct Control Health Monit*. 2017;24(3):e1879.
29. Wang F, Su W. Impact of inerter nonlinearities on vehicle suspension control. *Veh Syst Dyn*. 2008;46(7):575-595.
30. Shen Y, Chen L, Liu Y, Zhang X. Modeling and optimization of vehicle suspension employing a nonlinear fluid inerter Shock and Vibration; 2016.
31. Moraes F, Silveira M, Gonċalves P.. On the dynamics of a vibration isolator with geometrically nonlinear inerter. *Nonlinear Dyn*. 2018;93(3):1325-1340.
32. Bishop R. The treatment of damping forces in vibration theory. *Aeronautical J*. 1955;59(539):738-742.
33. Reid T. Free vibration and hysteretic damping. *Aeronautical J*. 1956;60(544):283-283.
34. Crandall S. Dynamic response of systems with structural damping. *Technical Report: Air Force Office of Scientific Research (AFOSR) 1561*, Massachusetts Institute of Technology Cambridge; 1961. http://hdl.handle.net/1721.1/100708
35. Chen L, Chen J, Chen C, Hong H. Free vibration of a SDOF system with hysteretic damping. *Mech Res Commun*. 1994;21(6):599-604.
36. Mastroddi F, Martarelli F, Eugeni M, Riso C. Time- and frequency-domain linear viscoelastic modeling of highly damped aerospace structures. *Mechanical Systems and Signal Processing*. 2019;2019(122):42-55.
37. Chopra AK. *Dynamics of Structures: Theory and Applications to Earthquake Engineering*. Boston: Pearson/Prentice Hall; 2007. ISBN 10: 0-13-285803-7. Boston, the United States of America.
38. Blandon C, Priestley M. Equivalent viscous damping equations for direct displacement based design. *J Earthq Eng*. 2005;9(2):257-278.
39. Makris N. Causal hysteretic element. *J Eng Mech*. 1997;123(11):1209-1214.
40. Muscolino G, Palmeri A, Ricciardelli F. Time-domain response of linear hysteretic systems to deterministic and random excitations. *Earthq Eng Struct Dyn*. 2005;34(9):1129-1147.
41. Inaudi J, Makris N. Time-domain analysis of linear hysteretic damping. *Earthq Eng Struct Dyn*. 1996;25(6):529-546.
42. Málaga-Chuquitaype C, Menendez-Vicente C, Thiers-Moggia R. Experimental and numerical assessment of the seismic response of steel structures with clutched inerters. *Soil Dyn Earthq Eng*. 2019;121:200-211.
43. Beards CF. *Structural Vibration*: Butterworth-Heinemann; 1996. ISBN 9780340645802.
44. lnaudi J, Kelly JM. *A Friction Mass Damper for Vibration Control*; Earthquake Engineering Research Center University of California at Berkeley; 1992.
45. Joseph R, Kirsten A, Scott C. Complex stiffness measurement of vibration damped structural elements. *Proc Int Modal Anal Conf*. 2000;1:391-397.
46. Mohan D, Scott G, Dave G. Measurement of dynamic parameters of automotive exhaust hangers. SAE Technical Papers. In: Noise and Vibration Conference and Exposition, Vol. 1; 2001:1-8.
47. Bloss B, Mohan D. Measurement of damping in structures by the power input method. *Exp Tech*. 2002;26(3):30-32.
48. Lu E, Zaidi M. Dynamic stiffness and loss factor measurement of engine rubber mount by impact test. *Mater Des*. 2011;32:1880-1887.
49. Wong W. Optimal design of a hysteretic vibration absorber using fixed-points theory. *J Acoust Soc Am*. 2016;139(6):3110-3115.
50. Makris N. Basic response functions of simple inertoelastic and inertoviscous models. *J Eng Mech*. 2017;143(11):04017123.
51. Makris N. Time-response functions of mechanical networks with inerters and causality. *Meccanica*. 2018;53:2237-2255.
52. Bae S, Cho J, Bae S, Jeong W. A discrete convolutional Hilbert transform with the consistent imaginary initial conditions for the time-domain analysis of five-layered viscoelastic sandwich beam. *Comput Methods Appl Mech Eng*. 2014;268:245-263.
53. Bae S, Cho J, Jeong W. Time-duration extended Hilbert transform superposition for the reliable time domain analysis of five-layered damped sandwich beams. *Finite Elem Anal Des*. 2014;90:41-49.
54. Bae S, Jeong W, Cho JR. Transient response of complex stiffness system using a green function from the Hilbert transform and the steady space technic,; 2014:3146-3155.
55. Bae S, Cho J, Jeong W. Free and transient responses of linear complex stiffness system by Hilbert transform and convolution integral. *Smart Struct Syst*. 2016;17(5):753-771.

56. Bae S, Jeong W, Cho J, Lee S. Transient response of vibration systems with viscous-hysteretic mixed damping using Hilbert transform and effective eigenvalues. *Smart Struct Syst*. 2017;20(3):263-272.
57. Qin A, Suganthan PN. Self-adaptive differential evolution algorithm for numerical optimization. In: 2005 IEEE Congress on Evolutionary Computation; 2005; Edinburgh, Scotland UK:2-5.
58. Storn R, Price K. Differential evolution—a simple and efficient heuristic for global optimization over continuous spaces. *J Glob Optim*. 1997;11:341-359.

How to cite this article: Deastra P, Wagg D, Sims N, Akbar M. Tuned inerter dampers with linear hysteretic damping. *Earthquake Engng Struct Dyn*. 2020;1-20. https://doi.org/10.1002/eqe.3287

APPENDIX A: COMPUTATIONAL ALGORITHM

As previously discussed, the main feature here is to obtain the solutions of the real and imaginary parts of both the modal responses in forward and reversed times from Equations (31) and (32). Herein, therefore, the process of Hilbert transformation is extremely important to obtain the accurate solutions.

Furthermore, as stated earlier, these state space equations need to satisfy the boundary conditions at $t = -\infty$ and $t = \infty$ in which both the displacement responses and forces are zeros. Therefore, for a finite time duration, nt, spans from an initial time, t_0, to an ending time, t_e, a numerical approximation is required to satisfy the boundary conditions. In the present work, it is defined that the force boundary conditions are

$$\mathbf{F_a}(-\infty) \approx \mathbf{F_a}(t_0 - nt) = 0 \tag{A1}$$

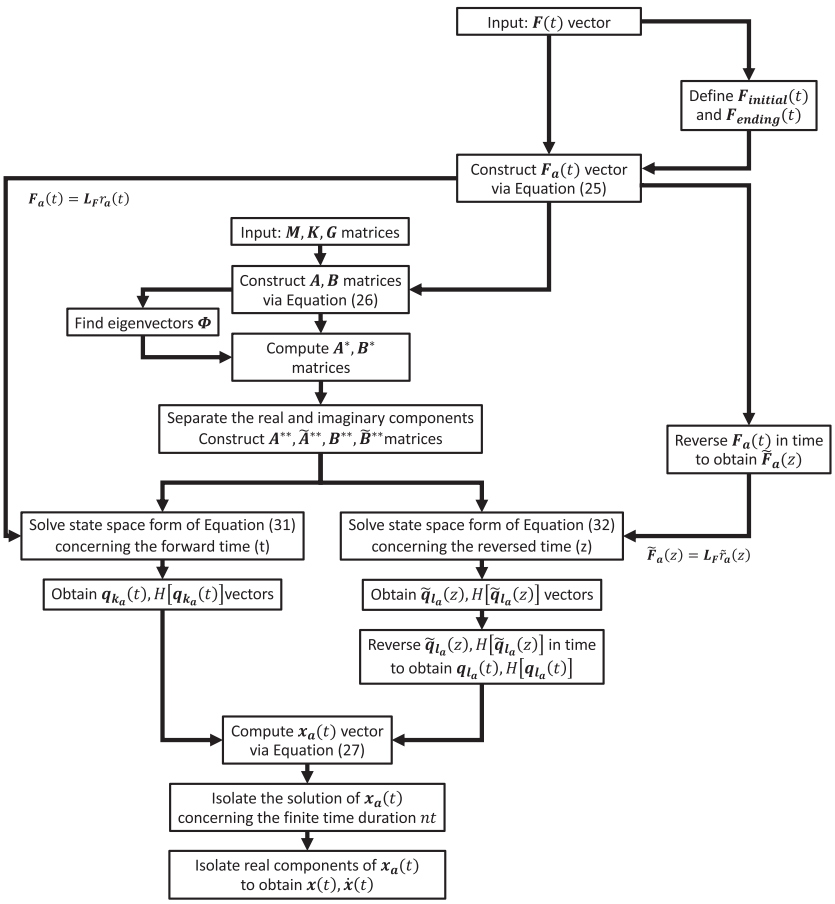

FIGURE A1 Computational algorithm

and

$$\mathbf{F_a}(\infty) \approx \mathbf{F_a}(t_e + nt) = 0, \tag{A2}$$

where $nt = t_e - t_0$. This definition also similarly applies to the displacement boundary conditions. Hence, prior to the Hilbert transformation of the original force vector, $\mathbf{F}$, "dummy" initial and ending conditions are added to the original force function. As an example, if $t_0 = 0s$ and $t_e = 100$ s, then the extended force function, F_{ext}, should span from $t = -100$ s to $t = 200$ s. This can be expressed as

$$\mathbf{F_{ext}}[(t_0 - nt) \rightarrow (t_e + nt)] = \mathbf{F_{initial}}[(t_0 - nt) \rightarrow t_0] + \mathbf{F}[t_0 \rightarrow t_e] + \mathbf{F_{ending}}[t_e \rightarrow (t_e + nt)], \tag{A3}$$

where the time parameters inside the square brackets define the time span of each force vector.

The "dummy" $F_{initial}$ and F_{ending} will depend to the shape of the original force function, $\mathbf{F}$. In the present case, if it is an impulse or random excitation force function, then $F_{initial}$ and F_{ending} are assumed to be zeros. However, if the original is a periodic function, that is, harmonic force function, $F_{initial}$ and F_{ending} need to be constructed as decaying functions such that their values at the time boundaries are zeros.

The next step is then to obtain the Hilbert transformation of the extended force function, F_{ext}. Thus, the earlier analytical force function as expressed in Equation (24) becomes

$$\mathbf{F_a}(t) = \mathbf{F_{ext}}(t) + j\ H[\mathbf{F_{ext}}(t)] \tag{A4}$$

and then flipped to obtain the reversed-time force function, that is, if $F_a(t)$ spans from -100 to 200 s, then $\tilde{\mathbf{F}}_\mathbf{a}(z)$ spans from 200 to -100s.

After the force function is constructed, the following steps are to construct the state space forms as given in Equations (31) and (32). The detailed algorithm of the present computational approach is depicted in Figure A1.

In the present work, a built-in Runge–Kutta module in MATLAB, so-called ODE45 module, is used to obtain the solutions of the sets of ordinary differential equations given in Equations (31) and (32). It is important to note that once the solutions of Equation (32) is obtained, it is still in the reversed time, z. Hence, the solutions needs to be reversed back to the original time, t, as depicted in Figure A1.

Once the modal responses vectors, $\mathbf{q_{k_a}}(t)$ and $\mathbf{q_{l_a}}(t)$, are computed, then the displacement-velocity vector, $x_a(t)$, can be calculated via Equation (23). The solutions are then isolated for the finite duration time, nt. The real parts of the solutions are the actual responses, $\mathbf{x}(t), \dot{\mathbf{x}}(t)$, of the system due to the force $\mathbf{F}(t)$.